ChemPhysChem

Research Article
doi.org/10.1002/cphc.202100831

Chemistry Europe
European Chemical Societies Publishing

www.chemphyschem.org

DFT Calculations for Mössbauer Properties on Dinuclear Center Models of the Resting Oxidized Cytochrome *c* Oxidase

Wen-Ge Han Du,[a] Andreas W. Götz,[b] and Louis Noodleman*[a]

Mössbauer isomer shift and quadrupole splitting properties have been calculated using the OLYP-D3(BJ) density functional method on previously obtained (W.-G. Han Du, et al., *Inorg Chem.* **2020**, *59*, 8906–8915) geometry optimized Fe_{a3}^{3+}–H_2O–Cu_B^{2+} dinuclear center (DNC) clusters of the resting oxidized (**O** state) "as-isolated" cytochrome *c* oxidase (CcO). The calculated results are highly consistent with the available experimental observations. The calculations have also shown that the structural heterogeneities of the **O** state DNCs implicated by the Mössbauer experiments are likely consequences of various factors, particularly the variable positions of the central H_2O molecule between the Fe_{a3}^{3+} and Cu_B^{2+} sites in different DNCs, whether or not this central H_2O molecule has H-bonding interaction with another H_2O molecule, the different spin states having similar energies for the Fe_{a3}^{3+} sites, and whether the Fe_{a3}^{3+} and Cu_B^{2+} sites are ferromagnetically or antiferromagnetically spin-coupled.

Introduction

Cytochrome *c* oxidases (CcOs) are the terminal electron acceptors in the respiratory chain of mitochondria and many bacteria.[1–3] These proteins reduce O_2 to H_2O and use the resulting energy to pump protons across the membrane. This produces the chemiosmotic proton gradient that is subsequently harnessed by ATP synthase to synthesize ATP.[4–8] The catalytic site of CcO that binds and reduces O_2 by $4e^-/4H^+$ transfer contains a heme a_3 (Fe_{a3}) and a Cu (Cu_B) ion that are in spatial vicinity (~5 Å distance). This Fe_{a3}–Cu_B active site is usually called the dinuclear (or binuclear) center/complex (DNC or BNC). In all types of CcO enzymes, the iron in the Fe_{a3} site is coordinated to heme and an axial histidine ligand (His384, residue numbers in this paper are by default for ba_3 CcO from *Thermus thermophilus* (*Tt*)). The copper in the Cu_B site is coordinated to three histidine ligands: His233, His282, and His283, where the His233 side chain is also covalently linked to the side chain of Tyr237. This special tyrosine side chain can be alternatively in neutral (Tyr–OH), deprotonated ionic (Tyr–O^-), or radical (Tyr–$O^\bullet$) states, and plays an important role in electron and proton transfer in the DNC.[9]

The oxidation, spin, and ligation states of the Fe_{a3} and Cu_B sites change during the catalytic cycle.[8–19] Although many insights into the intermediate states of the DNC in the catalytic cycle have been obtained (Figure 1) (see review articles[8,10,11] and the references therein), the detailed DNC structure of the resting oxidized as-isolated CcO state (state **O**) has been under debate for over 20 years despite various spectral and structural analyses that have been made.[20–28]

The electron density lying directly between Fe_{a3} and Cu_B in the as-isolated oxidized aa_3 type CcOs from *Paracoccus denitrificans* (*Pd*) and *Rhodobacter sphaeroides* (*Rs*) was initially interpreted as a H_2O and OH^- ligand pair.[21,22] Later, stronger and more compact electron density for a peroxide type dioxygen species (O1–O2) bridging the Fe_{a3} and Cu_B DNC was observed in higher resolution X-ray crystal structures of the oxidized CcOs from *Pd* (PDB code: 3HB3, 2.25 Å resolution),[23] from bovine heart (PDB code: 2ZXW, 1.95 Å resolution),[24] and from ba_3 *Tt* (3S8G and 3S8F, 1.8 Å resolution).[25] Further, the peroxide type species in the resting oxidized DNC was also observed from analysis of an X-ray free-electron laser (XFEL) experiment (1.9 Å resolution),[26] and very recently from analysis of a single-particle cryo-electron microscopy (cryo-EM) experiment at similar resolution.[29] Different groups reported different O1–O2 distances from 1.4~1.7 Å. Recently, a single hydroxide or alternatively a single water molecule between the Fe_{a3} and Cu_B sites was reported in a radiation-damage-free oxidized ba_3 CcO structure (2.3 Å resolution) at room temperature.[27] However, analysis of very recent low-dose high-energy X-ray data on the oxidized-resting bovine heart CcO again showed a peroxide-shaped electron density between the Fe_{a3} and Cu_B sites.[28] Even at fairly high resolution currently available (1.9 Å), there is considerable uncertainty in the electron density

[a] *Dr. W.-G. Han Du, Prof. L. Noodleman*
Department of Integrative Structural and Computational Biology,
The Scripps Research Institute
10550 North Torrey Pines Road, La Jolla, CA 92037, USA
E-mail: lou@scripps.edu
[b] *Dr. A. W. Götz*
San Diego Supercomputer Center,
University of California San Diego
9500 Gilman Drive MC0505, La Jolla, CA 92093, USA

Supporting information for this article is available on the WWW under https://doi.org/10.1002/cphc.202100831

Part of the Chemistry Europe joint Special Collection on Quantum Bio-inorganic Chemistry.

© 2022 The Authors. ChemPhysChem published by Wiley-VCH GmbH. This is an open access article under the terms of the Creative Commons Attribution Non-Commercial License, which permits use, distribution and reproduction in any medium, provided the original work is properly cited and is not used for commercial purposes.

© 2022 The Authors. ChemPhysChem published by Wiley-VCH GmbH

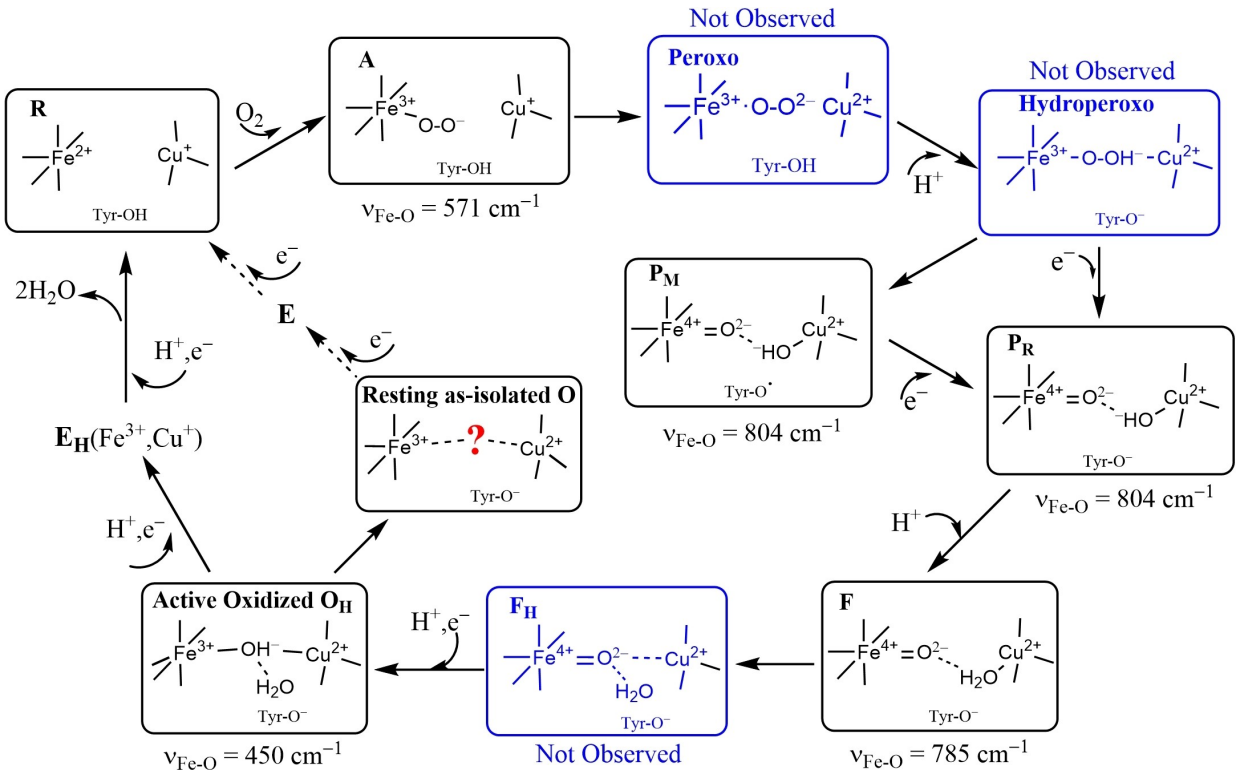

Figure 1. Feasible intermediate states of the DNC in the catalytic cycle, in which **A**, $\mathbf{P_M}$/$\mathbf{P_R}$, **F**, and $\mathbf{O_H}$ were identified by resonance Raman experiments,[8,10,11] and their DNC's are likely in the forms presented above.[18] Although the states in the blue frames were not observed experimentally, they may exist for a short time in the catalytic cycle.

between the metals, and in the correct modeling of the corresponding ligands, which are not clearly known prior to the fits. There is, in practice, both static and dynamic disorder in the ligand positions, typically represented by isotropic B factors. There is further disorder in the Fe and Cu positions as well. (While the variation in the Fe and Cu positions is expected to be geometrically smaller, they have much higher electron densities than di-oxygen or water species.) These B factors are variables with a potential range of values during the density fitting, and influence the final electron densities found.

In order to examine what species lies between the Fe_{a3}^{3+} and Cu_B^{2+} sites producing the apparent extended di-oxygen type electron density in the DNC of the oxidized as-isolated C*c*O, previously we have performed DFT calculations[30–32] on a series of DNC model clusters based on the X-ray crystal structure 3S8G[25] from *Tt ba3* C*c*O. Our calculations have shown that the observed di-oxygen species cannot be represented by O_2^{2-}, $O_2^{\bullet-}$, or H_2O_2, since the DFT optimized structures with bridging O_2^{2-} or $O_2^{\bullet-}$ have large structural discrepancies compared with the X-ray crystal structure, and the H_2O_2 is not stable between the Fe_{a3}^{2+} and Cu_B^{+} sites (Fe_{a3}^{3+} and Cu_B^{2+} metal sites were assumed reduced in the synchrotron X-ray beam).[30] We initially came to the conclusion that the observed di-oxygen species was best represented as HO_2^-, which could be a product of the photoreaction of the H_2O/OH^- ligands in Fe_{a3}^{3+}–H_2O···OH^-–Cu_B^{2+}/Fe_{a3}^{3+}–OH^-···H_2O–Cu_B^{2+} type DNC structures with associated $2e^-$ transfer to the adjacent oxidized Fe_{a3}^{3+} and Cu_B^{2+} sites in the X-ray beam.[30] However, if the resting oxidized DNC structure is originally (before X-ray irradiation) in the Fe_{a3}^{3+}–H_2O···OH^-–Cu_B^{2+} or Fe_{a3}^{3+}–OH^-···H_2O–Cu_B^{2+} form, the X-ray crystallographic experiments should still show H_2O···OH^- as the dominant bridging species in the DNC with long O···O distance, 2.5 Å or greater. Because the X-ray crystal structure represents both a spatial and time average over many billions of enzyme molecules, while some effects due to the X-ray irradiation are probably observable with careful attention to the time course, these effects are not likely to be dominant averaged over billions of structural sites. These arguments are even stronger when applied to XFEL experiments, since the total radiation dose is much smaller than in synchrotron X-ray experiments, and the relevant time scale for diffraction is far shorter. Further, our very recent calculations have demonstrated that the Fe_{a3}^{3+}–H_2O···OH^-–Cu_B^{2+}/Fe_{a3}^{3+}–OH^-···H_2O–Cu_B^{2+} type structures are also unlikely to represent the resting state of the DNC, consistent with the structural evidence and analysis above.[32]

Our most recent calculations have shown that the observed peroxide type electron density between the two metal centers is probably a mistaken analysis due to superposition of the electron density of a water molecule located at alternative positions between Fe_{a3}^{3+} and Cu_B^{2+} sites in DNC's of different C*c*O molecules.[32] Our calculations indicate that the H_2O molecule in the resting state **O**[Fe_{a3}^{3+}–H_2O–Cu_B^{2+}] DNC structures can bind with either the Fe_{a3}^{3+} or the Cu_B^{2+} site, or

© 2022 The Authors. ChemPhysChem published by Wiley-VCH GmbH

can reside at several positions between the Fe_{a3}^{3+} and Cu_B^{2+} sites that are all energetically similar, depending on the Fe_{a3}^{3+}–Cu_B^{2+} distance and H-bonding interaction with an additional H_2O molecule. (In our modeling, the latter water lies well off the direct line between the Fe and Cu ions.)[32] Figure 2 shows the overlap of the electron density map reconstructed from the X-ray crystal structure 3S8G[25] of *Tt* ba_3 and several of our geometry optimized **O**[Fe_{a3}^{3+}–H_2O–Cu_B^{2+}] DNC structures with very similar energies and with a H_2O molecule (in red) at different positions between the Fe_{a3}^{3+} and Cu_B^{2+} sites.[32] Because the diffraction pattern and the inferred electron density map represents the effective long-range order averaged over a large number molecules and unit cells in the X-ray structure, this averaging can result in an apparent observed superposition of water at different positions between the Fe_{a3}^{3+} and Cu_B^{2+} metal sites.

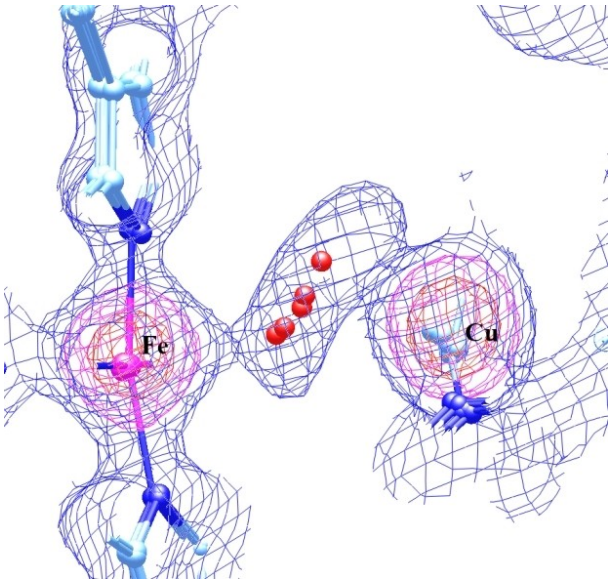

Figure 2. The overlap of the electron density map that was reconstructed from the oxidized as-isolated *Tt* ba_3 X-ray crystal structure 3S8G[25] data file with several of our calculated resting O state DNC structures, in which a water molecule (in red color) resides in different locations between the Fe_{a3}^{3+} and Cu_B^{2+} sites with very similar energies. Reprinted with permission from Figure 7 of Ref. [32], https://pubs.acs.org/doi/10.1021/acs.inorgchem.0c00724, Copyright (**2020**) American Chemical Society (further permissions for reusing this figure should be directed to the ACS).

Earlier ^{57}Fe Mössbauer experiments also demonstrated extensive structural and electronic heterogeneities in the DNC for the resting **O** state C*c*Os.[33–36] The major Mössbauer experimental observations on different C*c*Os are summarized in Table 1. Initial experiments on both *Tt* c_1aa_3 and bovine aa_3 show broad $^{57}Fe_{a3}$ spectra with isomer shift (δ) and quadrupole splitting (ΔE_Q) values averaged at ($\delta = 0.41\ mm\,s^{-1}$, $\Delta E_Q = 1.10\ mm\,s^{-1}$) and ($\delta = 0.48 \pm 0.06\ mm\,s^{-1}$, $\Delta E_Q = 1.0 \pm 0.1\ mm\,s^{-1}$), respectively.[33,34] These particular values show that the Fe_{a3}^{3+} site is in a high-spin (HS) state. Later, more complicated Mössbauer spectra were reported for *Tt* c_1aa_3 at different pH,[35] which showed that at least three HS–Fe_{a3}^{3+} species existed at pH = 5.7, and at least two HS–Fe_{a3}^{3+} complexes were observed at pH = 6.5, 7.8, and 9.3.[35] However, only one set of the HS parameters was defined at ($\delta = 0.41\ mm\,s^{-1}$, $\Delta E_Q = 1.3\ mm\,s^{-1}$). In addition, a "low-spin" (LS) Fe_{a3}^{3+} species was identified at pH = 5.7, 7.8, and 9.3 with the parameters ($\delta = 0.29\ mm\,s^{-1}$, $\Delta E_Q = 2.21\ mm\,s^{-1}$).[35] Note that this Fe_{a3}^{3+} species may be alternatively in an intermediate-spin (IS) state based on the observed isomer shift and quadrupole splitting values. Further, more complex Fe_{a3}^{3+} species which were temperature-dependent in *Tt* ba_3 were also observed in Mössbauer experiments.[36] Briefly, a HS–Fe_{a3}^{3+} species with ($\delta = 0.41\ mm\,s^{-1}$, $\Delta E_Q = 0.71\ mm\,s^{-1}$) and a LS–$Fe_{a3}^{3+}$ (which may be an IS state instead) with ($\delta = 0.29\ mm\,s^{-1}$, $\Delta E_Q = 2.24\ mm\,s^{-1}$) coexisted at 4.2 K.[36] When the temperature was increased above 190 K, the "LS–Fe_{a3}^{3+} species" began to transform to a different HS species with $\Delta E_Q \approx 1\ mm\,s^{-1}$. The δ value of this HS- Fe_{a3}^{3+} species was not specifically reported. But from the context, we assume that it had the same value of $\delta = 0.41\ mm\,s^{-1}$ as the other HS species. (Otherwise, the fit for the new HS species would have required a different isomer shift value from the other HS state.) The LS→HS transformation is

Table 1. Experimentally observed[33–36] $^{57}Fe_{a3}^{3+}$ Mössbauer isomer shifts (δ, $mm\,s^{-1}$) and quadrupole splittings (ΔE_Q, $mm\,s^{-1}$) in different resting oxidized cytochrome oxidases.

Oxidases	Ref.	Fe_{a3}^{3+}-Spin[a]	*T* [K]	δ	ΔE_Q	Note
Tt c_1aa_3	[33]	HS	4.2	0.41	1.10	The parameters given are averaged values. The spectrum is broad, suggesting heterogeneities.
bovine aa_3	[34]	HS	4.2	0.48 ± 0.06	1.0 ± 0.1	The a_3 sites also appear to be heterogeneous. The parameters reported are also averaged values.
Tt c_1aa_3	[35]	HS	4.2	0.41	1.3	Only one set of the HS parameters was defined. However, at least 3 and 2 HS a_3 species were observed at pH = 5.7 and pH = (6.5, 7.8, 9.3), respectively. And the LS a_3 species was found at pH = 5.7, 7.8, and 9.3.
		LS [b]	4.2	0.29	2.21	
Tt ba_3	[36]	HS	4.2–245	0.41	0.7	The first two HS and LS species coexist at 4.2 K. However, the LS component changes to a different HS species with $\Delta E_Q \approx 1\ mm\,s^{-1}$ when $T > 190$ K, and the transition is complete at 245 K.
		LS [b]	4.2–190	0.29	2.24	
		HS	> 190	0.41 [c]	~1	

[a] HS stands for high-spin; IS is for intermediate-spin; and LS is for low-spin. [b] Although it was suggested as LS–Fe_{a3}^{3+}, it is not certain whether it is LS or IS Fe_{a3}^{3+} site. [c] This δ value was not specifically reported in the paper.[36] However, from the context, we assume it is the same as another HS species, $0.41\ mm\,s^{-1}$.

© 2022 The Authors. ChemPhysChem published by Wiley-VCH GmbH

finished at 245 K. Therefore, the two different HS–Fe_{a3}^{3+} species coexisted at 245 K.[36]

In our recent publication,[32] we have calculated **O** state Fe_{a3}^{3+}–H_2O–Cu_B^{2+} DNC structures with Fe_{a3}^{3+} in HS, IS, and LS states. The $Fe_{a3}^{HS,3+}$–H_2O–Cu_B^{2+} results were presented in the main text, while the $Fe_{a3}^{IS,3+}$–H_2O–Cu_B^{2+} and $Fe_{a3}^{LS,3+}$–H_2O–Cu_B^{2+} results have been given in the Supporting Information.[32] Further, our calculations have also shown that the spin coupling between the Fe_{a3}^{3+} and Cu_B^{2+} sites appears very weak. For a given **O** state Fe_{a3}^{3+}–H_2O–Cu_B^{2+} DNC structure, similar energies are obtained whether Fe_{a3}^{3+}–Cu_B^{2+} are ferromagnetically (F) or anti-ferromagnetically (AF) coupled. In the current paper, based on the geometries we obtained for the **O**[$Fe_{a3}^{HS/IS/LS,3+}$–H_2O–Cu_B^{2+}] DNC structures,[32] we will calculate their $^{57}Fe_{a3}^{3+}$ Mössbauer isomer shift and quadrupole splitting properties and see how the calculated values correlate with the experimental observations. In contrast to the X-ray structures derived using synchrotron X-ray beams, or XFEL pulses, Mossbauer gamma rays give far less intense radiation, so the resting **O** states and their structures will not be sensitive to the gamma irradiation.

The Calculated O State $Fe_{a3}^{HS/IS/LS,3+}$–H_2O–Cu_B^{2+} DNC Structures

Our calculated **O**[$Fe_{a3}^{HS/IS/LS,3+}$–H_2O–Cu_B^{2+}] DNC structures are taken from our recent publication Ref. [32]. The initial geometries of the DNC model clusters were established based on the Cartesian coordinates of the *ba*$_3$ *Cc*O X-ray crystal structure 3S8G.[25] Then geometry optimization calculations were performed using DFT broken-symmetry[37–39]/OLYP-D3(BJ)[40]/Triple-ξ-Polarization(TZP) plus COSMO[17,18,41–44] solvation model methodology implemented within the ADF2017 software package.[45–47] The inclusion of dispersion D3(BJ) force-field type effects on the geometries distinguishes our current Mossbauer calculations from those we performed previously both for the fit set of Fe structure complexes (see section $^{57}Fe_{a3}^{3+}$ Mössbauer Isomer Shift and Quadrupole Splitting Calculations), and for the **O** state structures. The inner cores of C(1s), N(1s), and O(1s) were treated by frozen core approximation during geometry optimizations. Several $Fe_{a3}^{HS/IS/LS,3+}$–H_2O–Cu_B^{2+} local minima were found with the H_2O molecule residing at different positions between Fe_{a3}^{3+} and Cu_B^{2+}. Specifically, one structure for the $Fe_{a3}^{LS,3+}$–H_2O–Cu_B^{2+} state and four structures (noted as a, b, c, and d) for each of the $Fe_{a3}^{HS,3+}$–H_2O–Cu_B^{2+} and $Fe_{a3}^{IS,3+}$–H_2O–Cu_B^{2+} states were presented in our publication Ref. [32], and now are given in Table 2. For each broken-symmetry optimized geometry, we have also performed an Fe_{a3}^{3+}–Cu_B^{2+} F-coupled single-point energy calculation and have presented the relative energies in Table 2.

The four HS–Fe_{a3}^{3+} structures $Fe_{a3}^{HS,3+}$–H_2O–Cu_B^{2+}(a–d) are very similar to the corresponding IS–Fe_{a3}^{3+} structures $Fe_{a3}^{IS,3+}$–H_2O–Cu_B^{2+}(a–d). Further, the optimized $Fe_{a3}^{LS,3+}$–H_2O–Cu_B^{2+} structure is also similar to $Fe_{a3}^{HS/IS,3+}$–H_2O–Cu_B^{2+}(a) structures. The full model cluster representing the $Fe_{a3}^{HS,3+}$–H_2O–Cu_B^{2+}(a), $Fe_{a3}^{IS,3+}$–H_2O–Cu_B^{2+}(a), and the $Fe_{a3}^{LS,3+}$–H_2O–Cu_B^{2+} state is shown in Figure 3, in which the H_2O molecule is much closer to the Fe_{a3}^{3+} site with the distances (see Table 2) r(Fe_{a3}^{3+}–O) = 2.39, 2.40, and 2.37 Å and r(Cu_B^{2+}–O) = 2.94, 2.90, and 3.10 Å for the $Fe_{a3}^{HS,3+}$–H_2O–Cu_B^{2+}(a), $Fe_{a3}^{IS,3+}$–H_2O–Cu_B^{2+}(a), and $Fe_{a3}^{LS,3+}$–H_2O–Cu_B^{2+} structures, respectively. The H_2O molecule is also H-bonding with another H_2O molecule which probably originates from the Cu_B-bound H_2O ligand in the prior reaction cycle state **F** (see Figure 1). For a clearer view, the top and the central portions of this structure are also given in Figure 4. The central portions of the $Fe_{a3}^{HS/IS,3+}$–H_2O–Cu_B^{2+}(b–c) are also shown in Figure 4.

Table 2. OLYP-D3-BJ calculated distances (in Å), relative energies (ΔE, in kcal mol^{-1}), Mössbauer isomer shift (δ, in mm s^{-1}) and quadrupole splitting (ΔE_Q, in mm s^{-1}) values of the resting as-isolated Fe_{a3}^{3+}–H_2O–Cu_B^{2+} optimized DNC structures with different Fe_{a3}^{3+}–Cu_B^{2+} spin states.

Fe_{a3}^{3+}-Spin[a]	Structure	Distances [Å] Distances Fe–O	Cu–O	Fe···Cu	Spin-Coupling	ΔE	δ	ΔE_Q
HS	$Fe_{a3}^{HS,3+}$–H_2O–Cu_B^{2+}(a)	2.39	2.94	4.98	AF	0.0	0.40	0.80
					F	0.0	0.41	0.80
	$Fe_{a3}^{HS,3+}$–H_2O–Cu_B^{2+}(b)	2.47	2.77	4.90	AF	−0.2	0.41	0.92
					F	−0.2	0.41	0.80
	$Fe_{a3}^{HS,3+}$–H_2O–Cu_B^{2+}(c)	3.55	2.21	4.73	AF	0.3	0.43	0.78
					F	−0.4	0.45	1.21
	$Fe_{a3}^{HS,3+}$–H_2O–Cu_B^{2+}(d)	3.26	2.20	4.73	AF	0.5	0.41	0.77
					F	0.3	0.43	1.24
IS	$Fe_{a3}^{IS,3+}$–H_2O–Cu_B^{2+}(a)	2.40	2.90	4.94	AF	−6.2	0.36	2.42
					F	−6.2	0.36	2.42
	$Fe_{a3}^{IS,3+}$–H_2O–Cu_B^{2+}(b)	2.46	2.67	4.78	AF	−6.5	0.36	2.50
					F	−6.5	0.36	2.50
	$Fe_{a3}^{IS,3+}$–H_2O–Cu_B^{2+}(c)	3.44	2.26	4.71	AF	−4.3	0.34	2.34
					F	−4.1	0.34	2.33
	$Fe_{a3}^{IS,3+}$–H_2O–Cu_B^{2+}(d)	3.00	2.24	4.56	AF	−5.5	0.35	2.66
					F	−5.5	0.35	2.65
LS	$Fe_{a3}^{LS,3+}$–H_2O–Cu_B^{2+}	2.37	3.10	5.04	AF	−2.7	0.31	2.96
					F	−2.7	0.31	2.96

[a] HS stands for high-spin; IS is for intermediate-spin; and LS is for low-spin.

© 2022 The Authors. ChemPhysChem published by Wiley-VCH GmbH

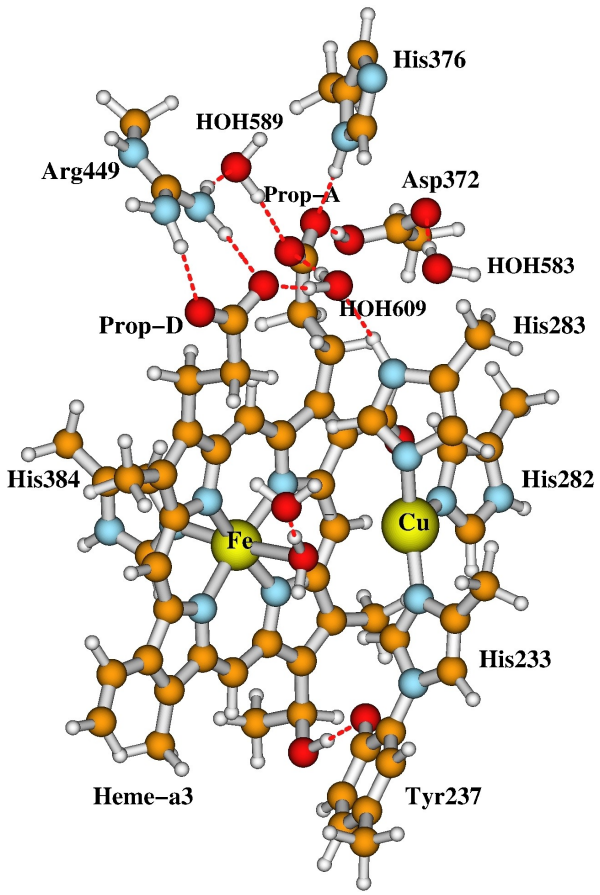

Figure 3. Our full DNC model cluster representing the $Fe_{a3}^{HS,3+}$–H_2O–Cu_B^{2+}(a), $Fe_{a3}^{IS,3+}$–H_2O–Cu_B^{2+}(a), and $Fe_{a3}^{LS,3+}$–H_2O–Cu_B^{2+} states, in which the H_2O molecule is much closer to the Fe_{a3}^{3+} site. The top and the central portions of the cluster are also shown in Figure 4. Linking hydrogen atoms were fixed during geometry optimization.

$^{57}Fe_{a3}^{3+}$ Mössbauer Isomer Shift and Quadrupole Splitting Calculations

In general, the isomer shifts (δ) can be calculated according to the fit equation [Eq. (1)]:

$$\delta = \alpha[\rho(0) - A] + C \quad (1)$$

where ρ(0) is the calculated electron density at Fe nucleus and A is a predefined constant close to the value of ρ(0). The parameters α and *C* are normally obtained by linear fitting between the calculated ρ(0) and the experimental (exp) δ values of a set of Fe^{2+}, Fe^{3+}, and Fe^{4+} complexes. However, we have found that a global fitting of a single equation for all $Fe^{2+,3+,4+}$ complexes in general underestimates the isomer shifts for the Fe^{2+} and Fe^{4+} sites, but overestimates the δ values for the Fe^{3+} state.[48–50] In order to reasonably predict the ^{57}Fe isomer shifts in different oxidation states, we have fit the parameters separately for the Fe^{2+} and for $Fe^{2.5+,3+,4+}$ complexes with PW91, OLYP, and OPBE functionals,[49,50] and have successfully predicted the isomer shifts for various states of the Fe–Fe, Fe–Mn, and Fe_4S_4 clusters in methane

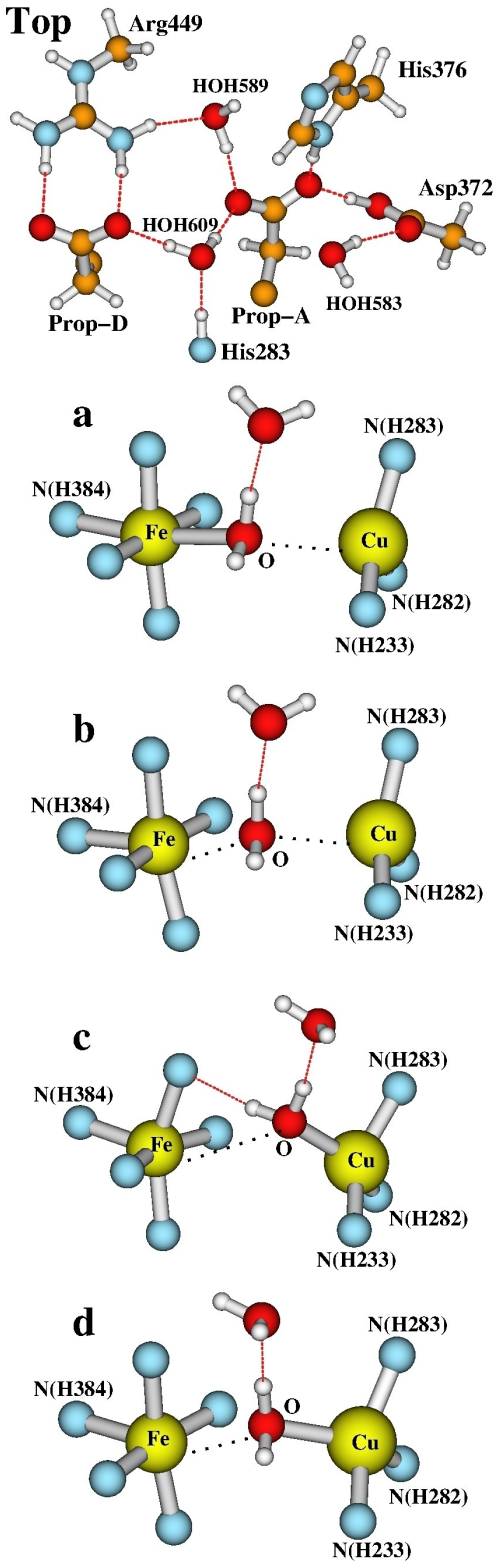

Figure 4. Four optimized **O** state DNC model clusters (noted as a, b, c, and d) for each of the $Fe_{a3}^{HS,3+}$–H_2O–Cu_B^{2+} and $Fe_{a3}^{IS,3+}$–H_2O–Cu_B^{2+} states and one structure for the $Fe_{a3}^{LS,3+}$–H_2O–Cu_B^{2+} state were presented in our publication Ref. [32]. Here is a closer look at the top and the central portions of these clusters. "a–d" show the central $Fe_{a3}^{HS/IS,3+}$–H_2O–Cu_B^{2+}(a–d) structures. "a" also represents the central portion of the $Fe_{a3}^{LS,3+}$–H_2O–Cu_B^{2+} model cluster. The Fe–O, Cu–O and Fe–Cu distances of the optimized $Fe_{a3}^{HS/IS,3+}$–H_2O–Cu_B^{2+}(a–d) and $Fe_{a3}^{LS,3+}$–H_2O–Cu_B^{2+} structures are given in Table 2. Relative energies of different states are reported in Tables 2 and 3.

© 2022 The Authors. ChemPhysChem published by Wiley-VCH GmbH

monooxygenase,[49–51] ribonucleotide reductases,[49,52–56] and APS-reductase.[57] We have also calculated the isomer shift and quadrupole splitting values with OLYP functional for the $Fe_{a3}^{2+/3+}$ site of ba_3 C*c*O based on several X-ray crystal structures.[31] However, at that time, we did not propose that a single water molecule resides between the Fe_{a3}^{3+} and Cu_B^{2+} sites in the DNC of oxidized as-isolated C*c*O. In the current paper, we have performed the $\rho(0)$ *vs.* δ_{exp} linear fitting for the OLYP-D3(BJ) potential on the same training set of the $Fe^{2.5+,3+,3.5+,4+}$ complexes as we have done for the PW91, OLYP, and OPBE potentials.[49,50] The training set contains 19 $Fe^{2.5+,3+,3.5+,4+}$ sample complexes with total 30 Fe sites. Previously, we used our own program to calculate the electron density $\rho(0)$ at the Fe nuclei. More recently, the ADF computer code package by default also reports the electron density at the nuclei. Based on their description, the electron density is not calculated exactly at the center of the nucleus. Instead, the electron density is calculated at sample points on a small spherical surface surrounding the center of a nucleus. The computed electron density in the output of ADF is the average electron density on these points. We now use that $\rho(0)$ in ADF output to perform the linear fitting and the isomer shift calculations. We note that this procedure bears a close resemblance to the actual physical change in electron density-nuclear contact interaction (effectively over a thin spherical shell) when the ^{57}Fe nucleus changes its radius and volume upon gamma ray excitation from the ground state (spin I = 1/2) to its excited state (with spin I = 3/2). This same excitation changes the shape of the ^{57}Fe nucleus from spherical to ellipsoidal. That change produces the quadrupole splitting in the Mossbauer spectrum.

The details of the $Fe^{2.5+,3+,3.5+,4+}$ complexes in the training set and the $\rho(0)$ *vs.* δ_{exp} linear regression are given in the Supporting Information. Briefly, by taking the constant A = 11820.0, our linear fitting for the OLYP-D3(BJ) potential yields [Eq. (2)]:

$$\delta(Fe^{2.5+,3+,3.5+,4+}) = -0.337[\rho(0) - 11820.0] + 0.571 \ (mm\ s^{-1}) \quad (2)$$

with correlation coefficient r = −0.946 and a standard deviation SD = 0.068 mm s^{-1}. We then performed single-point energy calculations on each of our optimized **O** state $Fe_{a3}^{HS/IS/LS,3+}$–H_2O–Cu_B^{2+} DNC model clusters in both broken-symmetry (representing Fe_{a3}^{3+}–Cu_B^{2+} AF-coupled state) and F-coupled states with all electron and all TZP basis set to obtain the $\rho(0)$ values and further predicted the $^{57}Fe_{a3}^{3+}$ isomer shift values based on Equation (2). The quadrupole splitting values (ΔE_Q) were also obtained from ADF output in these calculations.

Normally the calculated electric field gradient (EFG) tensors *V* at the Fe nucleus are diagonalized and the eigenvalues are reordered so that $|V_{zz}| \geq |V_{yy}| \geq |V_{xx}|$. The asymmetry parameter η is defined as [Eq. (3)]:

$$\eta = (V_{xx} - V_{yy})/V_{zz} \quad (3)$$

Then the ΔE_Q for ^{57}Fe of the nuclear excited state ($I = 3/2$) can be calculated as [Eq. (4)]:

$$\Delta E_Q = (^1/_2)eQV_{zz}(1 + \eta^2/3)^{1/2} \quad (4)$$

where *e* is the electrical charge of a positive electron, *Q* is the nuclear quadrupole moment of Fe. Recently, the ADF software package determines the ΔE_Q value using $Q = 0.16$ barn, the current best experimental value.

We have listed our calculated $^{57}Fe_{a3}^{3+}$ isomer shift and quadrupole splitting results for our **O** state $Fe_{a3}^{HS/IS/LS,3+}$–H_2O–Cu_B^{2+} DNC model clusters in Table 2.

Results and Discussion

Calculated Mössbauer Properties for the High-Spin–$Fe_{a3}^{3+,HS}$–H_2O–Cu_B^{2+}(a–d) DNC Model Clusters

First, we compare our calculated Mössbauer properties with experimental data for Fe_{a3}^{3+} in high-spin state. In Table 1, the observed isomer shift values for the $Fe_{a3}^{HS,3+}$ are around 0.41−0.48 mm s^{-1}. Our calculated $\delta(Fe_{a3}^{3+,HS})$ values (see Table 2) for our $Fe_{a3}^{HS,3+}$–H_2O–Cu_B^{2+}(a–d) DNC models are 0.40–0.45 mm s^{-1}, which are highly consistent with these experiments. The available observed $\Delta E_Q(Fe_{a3}^{3+,HS})_{exp}$ values for different C*c*Os are reported as 0.7, ~1, 1.0 ± 0.1, 1.10, and 1.3 mm s^{-1}, while our calculated $\Delta E_Q(Fe_{a3}^{3+,HS})$ values are 0.77, 0.78, 0.80, 0.92, 1.21, and 1.24 mm s^{-1}, which also match the experimental values very well.

Note that in our DNC models shown in Figures 3 and 4 and the corresponding calculation results in Table 2, there is another H_2O molecule, which likely originates from the Cu_B-bound H_2O ligand in state **F** (see Figure 1), and has H-bonding interaction with the central H_2O molecule. In the X-ray crystal structure 3S8G,[25] a water molecule (HOH608) was seen 3.01 Å above one of the dioxygen atoms that is closer to Cu_B. Therefore, the HOH608 may have H-bonding interaction with the H_2O ligand in a position similar to Fe_{a3}^{3+}–H_2O–Cu_B^{2+}(c) (Figure 4c). No other H_2O molecules were identified within the H-bonding distances around the dioxygen in 3S8G. This probably implies that not all C*c*O molecules in the crystal have an H-bonding H_2O interacting with the central bridging H_2O molecule, and even if there is an H-bonding H_2O molecule in some of the C*c*O DNCs, the H-bonding patterns and the positions of the H-bonding H_2O molecules may differ, and therefore, they may not be identified in the X-ray crystal structure.

Since it is not clear whether there is an H-bonding H_2O molecule in the DNC of the **O** state, in our previous work in Ref. [32], we also performed broken-symmetry state geometry optimizations on the four $Fe_{a3}^{HS,3+}$–H_2O–Cu_B^{2+}(a)–(d) structures obtained by removing the H-bonding H_2O. The four corresponding optimized structures (S) were labeled as S1, S2, S3, and S4 in Figure 6 of Ref. [32], respectively. Their main bond distances and the calculated energies were given in Table 2 of Ref. [32], and are also given in Table 3 here, together with the single-point energy $Fe_{a3}^{HS,3+}$–Cu_B^{2+} F-coupled state calculations on the broken-symmetry optimized geometries.

© 2022 The Authors. ChemPhysChem published by Wiley-VCH GmbH

Table 3. OLYP-D3-BJ calculated properties (relative energies ΔE in kcal mol^{-1}, Mössbauer isomer shift δ in mm s^{-1}, quadrupole splitting ΔE_Q in mm s^{-1}) for the four geometry optimized high-spin–Fe_{a3}^{3+} DNC structures starting from $Fe_{a3}^{3+,HS}$–H_2O–Cu_B^{2+}(a–d) by deleting the H_2O molecule which has H-bonding interaction with the central H_2O molecule.[a]

Starting from Structure	Name in Ref. [32]	Optimized Geometry [Å]			Spin-Coupling	ΔE	δ	ΔE_Q
		Fe–O	Cu–O	Fe···Cu				
$Fe_{a3}^{HS,3+}$–H_2O–Cu_B^{2+}(a)	S1	2.61	2.82	5.03	AF	0.0	0.41	0.85
					F	0.0	0.41	0.86
$Fe_{a3}^{HS,3+}$–H_2O–Cu_B^{2+}(b)	S2	2.97	2.52	4.98	AF	−1.1	0.41	0.66
					F	−1.2	0.42	0.98
$Fe_{a3}^{HS,3+}$–H_2O–Cu_B^{2+}(c)	S3	3.54	2.29	4.76	AF	−1.5	0.42	0.60
					F	−1.9	0.44	1.09
$Fe_{a3}^{HS,3+}$–H_2O–Cu_B^{2+}(d)	S4	3.07	2.41	4.87	AF	−0.8	0.41	0.64
					F	−1.1	0.43	1.14

[a] These four geometry optimized structures (S) were given as S1, S2, S3, and S4, respectively, in Table 2 of Ref. [32].

Without the H-bonding H_2O molecule, the binding of the H_2O ligand with the two metal sites, especially with the $Fe_{a3}^{HS,3+}$ site, are weakened. But still the overlap of the S1–S4 structures with the DNC of 3S8G shows the H_2O molecules in S1–S4 reside along the apparent dioxygen species direction in 3S8G (see Figure 2). We therefore also calculated the $^{57}Fe_{a3}^{HS,3+}$ Mössbauer isomer shift and quadrupole splitting properties of these four structures in both AF- (broken-symmetry) and F-coupled states, and presented the results in Table 3. The calculated isomer shifts are almost the same as those given in Table 2, and are again highly consistent with the observed values.

Based on the calculated $^{57}Fe_{a3}^{HS,3+}$ Mössbauer properties given in Tables 2 and 3, it appears that the $^{57}Fe_{a3}^{HS,3+}$ isomer shifts only slightly vary with the position of the H_2O molecule, whether or not there is an H-bonding H_2O molecule, and whether $Fe_{a3}^{HS,3+}$ is F- or AF-coupled with Cu_B^{2+}. However, the $^{57}Fe_{a3}^{HS,3+}$ quadrupole splitting values are very sensitive to these factors. This explains that the observed Mössbauer spectra are broad, that the parameters are difficult to define precisely, and that many of the reported parameters are averaged values.[33–35] Our calculated *versus* the several reported experimentally defined $^{57}Fe_{a3}^{HS,3+}$ Mössbauer isomer shift and quadrupole splitting values are compared in Figure 5.

In general, when the H_2O molecule is much closer to the $Fe_{a3}^{HS,3+}$ site ($Fe_{a3}^{HS,3+}$–H_2O–Cu_B^{2+}(a)–(b)), the calculated $^{57}Fe_{a3}^{HS,3+}$ quadrupole splitting values for the F- and AF-coupled states are similar to each other. On the other hand, when the H_2O molecule is much closer to the Cu_B^{2+} site ($Fe_{a3}^{HS,3+}$–H_2O–Cu_B^{2+}(c)–(d)), the calculated $\Delta E_Q(Fe_{a3}^{HS,3+})$ values for the F-coupled state are much larger than the corresponding AF-coupled state. The observed $\Delta E_Q(Fe_{a3}^{HS,3+})_{exp}$ values around 1.0 to 1.3 mm s^{-1} (see Table 1)[33–36] likely arise from the DNC structures in which the H_2O molecule is much closer to the Cu_B^{2+} site and the $Fe_{a3}^{HS,3+}$ and Cu_B^{2+} sites are F-coupled (see Tables 2 and 3). Meanwhile, the observed $\Delta E_Q(Fe_{a3}^{HS,3+})_{exp}$ values around 0.7 mm s^{-1} probably come from the structures where the H_2O molecule is close to the $Fe_{a3}^{HS,3+}$ site (whether the $Fe_{a3}^{HS,3+}$ and Cu_B^{2+} sites are F- or AF-coupled), or from the structures where the H_2O molecule is much closer to Cu_B^{2+} and the two metal sites are AF-coupled.

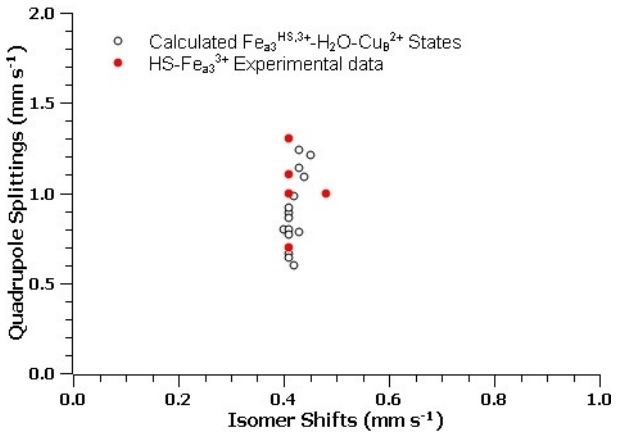

Figure 5. Calculated (black circles, data are given in Tables 2 and 3) *versus* several experimentally defined (red dots, data are given in Table 1) Mössbauer isomer shift and quadrupole splitting values for the high-spin (HS) $^{57}Fe_{a3}^{3+}$ site in *Cc*Os.

Calculated Mössbauer Properties for the Intermediate- and Low-Spin–$Fe_{a3}^{IS/LS,3+}$–H_2O–Cu_B^{2+} DNC Model Clusters

In *Tt* c_1aa_3 and ba_3 at certain pH or at low temperature (see Table 1),[35,36] a "low-spin" Fe_{a3}^{3+} species was observed with δ = 0.29 mm s^{-1} and ΔE_Q = 2.21/2.24 mm s^{-1}. Although this was proposed to be a low-spin Fe_{a3}^{3+} species, such δ and ΔE_Q values could also originate from an intermediate-spin Fe^{3+} site. Therefore, we have performed Mössbauer property calculations on our IS and LS $Fe_{a3}^{IS/LS,3+}$–H_2O–Cu_B^{2+} models listed in Table 2.

Unlike the high-spin–$Fe_{a3}^{HS,3+}$–H_2O–Cu_B^{2+} models, the F- and AF-coupled spin states yield essentially the same isomer shift and quadrupole splitting results for the same $Fe_{a3}^{IS/LS,3+}$–H_2O–Cu_B^{2+} structure. Further, the position of the H_2O molecule does not have significant effect on the calculated $^{57}Fe_{a3}^{IS,3+}$ isomer shift and quadrupole splitting values on the four $Fe_{a3}^{IS,3+}$–H_2O–Cu_B^{2+}(a)–(d) structures. Overall, the calculated $\delta(Fe_{a3}^{IS,3+})$ only varies from 0.34 to 0.36 mm s^{-1}, and $\Delta E_Q(Fe_{a3}^{IS,3+})$ from 2.33 to 2.66 mm s^{-1}.

For the low-spin–$Fe_{a3}^{LS,3+}$–H_2O–Cu_B^{2+} structure, our calculations give $\delta(Fe_{a3}^{LS,3+})$ = 0.31 mm s^{-1} and $\Delta E_Q(Fe_{a3}^{LS,3+})$ = 2.96 mm s^{-1}.

© 2022 The Authors. ChemPhysChem published by Wiley-VCH GmbH

Compared with experimental $\delta = 0.29\ mm\,s^{-1}$ and $\Delta E_Q = 2.21/2.24\ mm\,s^{-1}$ values, the calculated $\delta(Fe_{a3}{}^{LS,3+}) = 0.31\ mm\,s^{-1}$ is a little closer to experiment than the calculated $\delta(Fe_{a3}{}^{IS,3+})$ values (0.34 to 0.36 $mm\,s^{-1}$). However, the $\Delta E_Q(Fe_{a3}{}^{LS,3+}) = 2.96\ mm\,s^{-1}$ deviates more from experiment than the ΔE_Q-$(Fe_{a3}{}^{IS,3+})$ results (2.33 to 2.66) $mm\,s^{-1}$. In the Supporting Information, we have used linear regression on the training set of Fe complexes to find the standard deviation (SD) of the fit for the isomer shifts, SD = 0.068 $mm\,s^{-1}$, and also the standard deviation of the fit for the corresponding quadrupole splittings, SD = 0.30 $mm\,s^{-1}$. The experimentally observed Mössbauer spectrum with $\delta = 0.29\ mm\,s^{-1}$ and $\Delta E_Q = 2.21/2.24\ mm\,s^{-1}$ spectra has an isomer shift within 1 SD from either the DFT calculated low-spin or an intermediate-spin $Fe_{a3}{}^{3+}$ species. By contrast, for the predicted versus experimental quadrupole splitting, the calculated low-spin quadrupole splitting differs by more than 2 SD from experiment, while the calculated intermediate-spin quadrupole splittings are much closer < 1.5 SD.

In addition, the intermediate-spin $Fe_{a3}{}^{IS,3+}$–H_2O–$Cu_B{}^{2+}$(a)–(d) structures have lower energy than the low-spin $Fe_{a3}{}^{LS,3+}$–H_2O–$Cu_B{}^{2+}$ state, and the structure $Fe_{a3}{}^{IS,3+}$–H_2O–$Cu_B{}^{2+}$(c) has calculated $\delta = 0.34\ mm\,s^{-1}$ and $\Delta E_Q = 2.33\ mm\,s^{-1}$, which are the closest to the experiment. Therefore, the experimentally observed $\delta = 0.29\ mm\,s^{-1}$ and $\Delta E_Q = 2.21/2.24\ mm\,s^{-1}$ spectra are probably from intermediate-spin–$Fe_{a3}{}^{3+}$ DNCs.

Conclusions

In our previous study,[32] we proposed that a single water molecule is in between the $Fe_{a3}{}^{3+}$ and $Cu_B{}^{2+}$ sites in the resting oxidized as-isolated **O** state of C*c*O. Depending on the $Fe_{a3}{}^{3+}$–$Cu_B{}^{2+}$ distance and presence or absence of H-bonding to another H_2O molecule, this single H_2O molecule can coordinate to either the $Fe_{a3}{}^{3+}$ or the $Cu_B{}^{2+}$ site, or can reside at different positions between the $Fe_{a3}{}^{3+}$ and $Cu_B{}^{2+}$ sites that are energetically very close on the potential energy surface. We therefore have also proposed that the extended peroxide type electron density between $Fe_{a3}{}^{3+}$ and $Cu_B{}^{2+}$ observed in several C*c*O X-ray crystal structures[23–25] results are the consequence of the superposition of the electron density of a water molecule at different locations between $Fe_{a3}{}^{3+}$ and $Cu_B{}^{2+}$ in different C*c*O molecules within the crystals.

The structural heterogeneities of the DNC in the resting oxidized state C*c*Os (**O** state) were demonstrated by earlier $^{57}Fe^{3+}$ Mössbauer experiments,[33–36] in which the spectra were broad, the parameters were difficult to define precisely, and the reported parameters were averaged values.

In this paper, we have calculated the $^{57}Fe_{a3}{}^{3+}$ Mössbauer isomer shift (δ) and quadrupole splitting (ΔE_Q) properties of the resting state **O**[$Fe_{a3}{}^{3+}$–H_2O–$Cu_B{}^{2+}$] DNC structures that we obtained in Ref. [32], and have compared the calculated results with the available experimental values (see Table 1). Overall, the span of our calculated δ and ΔE_Q results for the high-spin–$Fe_{a3}{}^{3+}$ DNC structures agree very well with the experimental values. Our calculations show that the change of the high-spin-$^{57}Fe_{a3}{}^{3+}$ isomer shift among different DNC structures is within 0.05 $mm\,s^{-1}$. However, the quadrupole splitting values vary with the position of the central H_2O molecule, whether or not this H_2O molecule has H-bonding interaction with another H_2O molecule, and whether the high-spin–$Fe_{a3}{}^{3+}$ site is F- or AF-coupled with $Cu_B{}^{2+}$. The observed ΔE_Q values around 1.0 to 1.3 $mm\,s^{-1}$ (see Table 1)[33–36] likely result from the DNC structures in which the central H_2O molecule is much closer to the $Cu_B{}^{2+}$ site and the high-spin–$Fe_{a3}{}^{3+}$ and $Cu_B{}^{2+}$ sites are F-coupled. Meanwhile the observed ΔE_Q values around 0.7 $mm\,s^{-1}$ probably result from the structures where the H_2O molecule is close to the high-spin–$Fe_{a3}{}^{3+}$ site with the two metal sites either F- or AF-coupled, or from the structures where the H_2O molecule is much closer to $Cu_B{}^{2+}$ and the two metal sites are AF-coupled.

Our calculations also show that the observed "low-spin" $Fe_{a3}{}^{3+}$ species with $\delta = 0.29\ mm\,s^{-1}$ and $\Delta E_Q = 2.21/2.24\ mm\,s^{-1}$ more probably arises from an intermediate-spin–$Fe_{a3}{}^{3+}$ state, which exists at low temperature[36] or is more populated at certain pH values.[35]

Overall, our calculations demonstrate that the structural heterogeneities of the resting as-isolated oxidized state observed in several Mössbauer properties experiments are very consistent with the DFT predicted properties and structures of a single H_2O molecule bridging the $Fe_{a3}{}^{3+}$ and $Cu_B{}^{2+}$ sites with variable positions, with further variations explained by the $Fe_{a3}{}^{3+}$ spin states, and by the different spin-couplings between $Fe_{a3}{}^{3+}$ and $Cu_B{}^{2+}$.

Supporting Information

The details of the Mössbauer isomer shift parameters fitting for the OLYP-D3(BJ) functional, the $Fe^{2.5+,3+,3.5+,4+}$ complexes in the training set, and the $\rho(0)$ *vs.* δ_{exp} linear regression plots are given in the Supporting Information.

Acknowledgments

We thank NIH for financial support (R01GM100934) and thank The Scripps Research Institute for computational resources. This work also used the Extreme Science and Engineering Discovery Environment (XSEDE), which is supported by National Science Foundation (grant number ACI-1053575, resources at the San Diego Supercomputer Center through award TG-CHE130010 to AWG). We greatly appreciate highly valuable discussions with Duncan McRee and Ying Chen from our Scripps Research group, and with Tzanko Doukov and Aina Cohen from SSRL on X-ray structural issues related to this work.

Conflict of Interest

The authors declare no conflict of interest.

© 2022 The Authors. ChemPhysChem published by Wiley-VCH GmbH

Data Availability Statement

The data that support the findings of this study are available in the supplementary material of this article.

Keywords: cytochrome *c* oxidase · resting state · Mössbauer · isomer shift · quadrupole splitting

[1] O. M. H. Richter, B. Ludwig, *Rev. Physiol. Biochem. Pharmacol.* **2003**, *147*, 47–74.
[2] G. T. Babcock, M. Wikström, *Nature* **1992**, *356*, 301–309.
[3] S. Ferguson-Miller, G. T. Babcock, *Chem. Rev.* **1996**, *96*, 2889–2907.
[4] M. Wikström, *Biochim. Biophys. Acta* **2012**, *1817*, 468–475.
[5] V. R. I. Kaila, M. I. Verkhovsky, M. Wikström, *Chem. Rev.* **2010**, *110*, 7062–7081.
[6] A. A. Konstantinov, *FEBS Lett.* **2012**, *586*, 630–639.
[7] C. von Ballmoos, P. Adelroth, R. B. Gennis, P. Brzezinski, *Biochim. Biophys. Acta Bioenerg.* **2012**, *1817*, 650–657.
[8] M. Wikström, K. Krab, V. Sharma, *Chem. Rev.* **2018**, *118*, 2469–2490.
[9] M. R. A. Blomberg, *Front. Chem.* **2021**, *9*, 640155.
[10] S. Yoshikawa, A. Shimada, *Chem. Rev.* **2015**, *115*, 1936–1989.
[11] I. Ishigami, M. Hikita, T. Egawa, S. R. Yeh, D. L. Rousseau, *Biochim. Biophys. Acta Bioenerg.* **2015**, *1847*, 98–108.
[12] M. R. A. Blomberg, P. E. M. Siegbahn, *Biochim. Biophys. Acta Bioenerg.* **2015**, *1847*, 364–376.
[13] M. R. A. Blomberg, P. E. M. Siegbahn, *Biochim. Biophys. Acta Bioenerg.* **2015**, *1847*, 1173–1180.
[14] M. R. A. Blomberg, P. E. M. Siegbahn, *Biochim. Biophys. Acta* **2012**, *1817*, 495–505.
[15] L. Noodleman, W.-G. Han Du, J. A. Fee, A. W. Götz, R. C. Walker, *Inorg. Chem.* **2014**, *53*, 6458–6472.
[16] W.-G. Han Du, A. W. Götz, L. H. Yang, R. C. Walker, L. Noodleman, *Phys. Chem. Chem. Phys.* **2016**, *18*, 21162–21171.
[17] W.-G. Han Du, A. W. Götz, L. Noodleman, *Inorg. Chem.* **2018**, *57*, 1048–1059.
[18] W.-G. Han Du, A. W. Götz, L. Noodleman, *Inorg. Chem.* **2019**, *58*, 13933–13944.
[19] L. Noodleman, W.-G. Han Du, D. McRee, Y. Chen, T. Goh, A. W. Götz, *Phys. Chem. Chem. Phys.* **2020**, *22*, 26652–26668.
[20] A. J. Moody, *Biochim. Biophys. Acta Bioenerg.* **1996**, *1276*, 6–20.
[21] C. Ostermeier, A. Harrenga, U. Ermler, H. Michel, *Proc. Natl. Acad. Sci. USA* **1997**, *94*, 10547–10553.
[22] L. Qin, C. Hiser, A. Mulichak, R. M. Garavito, S. Ferguson-Miller, *Proc. Natl. Acad. Sci. USA* **2006**, *103*, 16117–16122.
[23] J. Koepke, E. Olkhova, H. Angerer, H. Muller, G. H. Peng, H. Michel, *Biochim. Biophys. Acta* **2009**, *1787*, 635–645.
[24] H. Aoyama, K. Muramoto, K. Shinzawa-Itoh, K. Hirata, E. Yamashita, T. Tsukihara, T. Ogura, S. Yoshikawa, *Proc. Natl. Acad. Sci. USA* **2009**, *106*, 2165–2169.
[25] T. Tiefenbrunn, W. Liu, Y. Chen, V. Katritch, C. D. Stout, J. A. Fee, V. Cherezov, *PLoS One* **2011**, *6*, e22348.
[26] K. Hirata, K. Shinzawa-Itoh, N. Yano, S. Takemura, K. Kato, M. Hatanaka, K. Muramoto, T. Kawahara, T. Tsukihara, E. Yamashita, K. Tono, G. Ueno, T. Hikima, H. Murakami, Y. Inubushi, M. Yabashi, T. Ishikawa, M. Yamamoto, T. Ogura, H. Sugimoto, J. R. Shen, S. Yoshikawa, H. Ago, *Nat. Methods* **2014**, *11*, 734–U174.
[27] R. Andersson, C. Safari, R. Dods, E. Nango, R. Tanaka, A. Yamashita, T. Nakane, K. Tono, Y. Joti, P. Bath, E. Dunevall, R. Bosman, O. Nureki, S. Iwata, R. Neutze, G. Branden, *Sci. Rep.* **2017**, *7*, 4518.
[28] G. Ueno, A. Shimada, E. Yamashita, K. Hasegawa, T. Kumasaka, K. Shinzawa-Itoh, S. Yoshikawa, T. Tsukihara, M. Yamamoto, *J. Synchrotron Radiat.* **2019**, *26*, 912–921.
[29] F. Kolbe, S. Safarian, Z. Piorek, S. Welsch, H. Muller, H. Michel, *Nat. Commun.* **2021**, *12*, 6903.
[30] W.-G. Han Du, L. Noodleman, *Inorg. Chem.* **2013**, *52*, 14072–14088.
[31] W.-G. Han Du, L. Noodleman, *Inorg. Chem.* **2015**, *54*, 7272–7290.
[32] W.-G. Han Du, D. McRee, A. W. Götz, L. Noodleman, *Inorg. Chem.* **2020**, *59*, 8906–8915.
[33] T. A. Kent, E. Munck, W. R. Dunham, W. F. Filter, K. L. Findling, T. Yoshida, J. A. Fee, *J. Biol. Chem.* **1982**, *257*, 12489–12492.
[34] T. A. Kent, L. J. Young, G. Palmer, J. A. Fee, E. Munck, *J. Biol. Chem.* **1983**, *258*, 8543–8546.
[35] F. M. Rusnak, E. Munck, C. I. Nitsche, B. H. Zimmermann, J. A. Fee, *J. Biol. Chem.* **1987**, *262*, 16328–16332.
[36] B. H. Zimmermann, C. I. Nitsche, J. A. Fee, F. Rusnak, E. Munck, *Proc. Natl. Acad. Sci. USA* **1988**, *85*, 5779–5783.
[37] L. Noodleman, *J. Chem. Phys.* **1981**, *74*, 5737–5743.
[38] L. Noodleman, D. A. Case, *Adv. Inorg. Chem.* **1992**, *38*, 423–470.
[39] L. Noodleman, T. Lovell, W.-G. Han, T. Liu, R. A. Torres, F. Himo, in: *Comprehensive Coordination Chemistry II, From Biology to Nanotechnology*, ed. A. B. Lever, Elsevier Ltd, **2003**, vol. *2*, pp. 491–510.
[40] S. Grimme, S. Ehrlich, L. Goerigk, *J. Comput. Chem.* **2011**, *32*, 1456–1465.
[41] A. Klamt, G. Schüürmann, *J. Chem. Soc. Perkin Trans. 2* **1993**, 799–805.
[42] A. Klamt, *J. Phys. Chem.* **1995**, *99*, 2224–2235.
[43] A. Klamt, V. Jonas, *J. Chem. Phys.* **1996**, *105*, 9972–9981.
[44] C. C. Pye, T. Ziegler, *Theor. Chem. Acc.* **1999**, *101*, 396–408.
[45] *ADF, Amsterdam Density Functional Software*, SCM, Theoretical Chemistry, Vrije Universiteit, Amsterdam, The Netherlands. http://www.scm.com.
[46] G. te Velde, F. M. Bickelhaupt, E. J. Baerends, C. F. Guerra, S. J. A. Van Gisbergen, J. G. Snijders, T. Ziegler, *J. Comput. Chem.* **2001**, *22*, 931–967.
[47] C. F. Guerra, O. Visser, J. G. Snijders, G. te Velde, E. J. Baerends, in: *Methods and techniques for computational chemistry*, eds. E. Clementi, C. Corongiu, STEF, Cagliari, **1995**, pp. 303–395.
[48] T. Liu, T. Lovell, W.-G. Han, L. Noodleman, *Inorg. Chem.* **2004**, *43*, 6858–6858.
[49] W.-G. Han, T. Liu, T. Lovell, L. Noodleman, *J. Comput. Chem.* **2006**, *27*, 1292–1306.
[50] W.-G. Han, L. Noodleman, *Inorg. Chim. Acta* **2008**, *361*, 973–986.
[51] W.-G. Han, L. Noodleman, *Inorg. Chem.* **2008**, *47*, 2975–2986.
[52] W.-G. Han, L. Noodleman, *Dalton Trans.* **2009**, 6045–6057.
[53] W.-G. Han, D. A. Giammona, D. Bashford, L. Noodleman, *Inorg. Chem.* **2010**, *49*, 7266–7281.
[54] W.-G. Han, L. Noodleman, *Theor. Chem. Acc.* **2010**, *125*, 305–317.
[55] W.-G. Han, L. Noodleman, *Inorg. Chem.* **2011**, *50*, 2302–2320.
[56] W.-G. Han, G. M. Sandala, D. A. Giammona, D. Bashford, L. Noodleman, *Dalton Trans.* **2011**, *40*, 11164–11175.
[57] D. P. Bhave, W.-G. Han, S. Pazicni, J. E. Penner-Hahn, K. S. Carroll, L. Noodleman, *Inorg. Chem.* **2011**, *50*, 6610–6625.

Manuscript received: November 19, 2021
Revised manuscript received: February 3, 2022
Accepted manuscript online: February 10, 2022
Version of record online: March 1, 2022

© 2022 The Authors. ChemPhysChem published by Wiley-VCH GmbH